Chapter 6

Evidence of distinct (nonpolar/polar) ordering at long/short ranges in relaxor ferroelectrics

6.1 Introduction

Various properties of perovskite-based smart materials can be tuned by engineering atomic ordering at various length scales. Among perovskite-based smart materials, relaxor ferroelectrics (or relaxors) are widely studied for their numerous applications *viz.*, electrical energy storage systems, sensors & actuators, medical ultrasonic imaging, and many more [5, 117]. The relaxors possess distinct structures at long- and short ranges, responsible for various fascinating properties. Unlike ordered systems, relaxor ferroelectrics such as $PbMg_{1/3}Nb_{2/3}O_3$ (PMN) [131], $PbSc_{1/2}Ta_{1/2}O_3$ [309], $PbZn_{1/3}Nb_{2/3}O_3$ (PZN) [310], etc., exhibit chemical heterogeneity that leads to disorder resulting in enhanced physical responses [5, 117]. The relaxor behavior is often linked with the presence of polar nano regions (PNRs), which nucleate and start growing below the Burns temperature (T_B)

[5, 137, 141]. The presence of PNRs and their interactions are held responsible for various physical properties observed in the relaxor material [5, 142].

Among various intriguing properties exhibited by perovskite-based oxides, controlled thermal expansion/Negative Thermal Expansion (NTE) is scientifically and technologically important [281, 282, 283, 284]. NTE/ZTE in perovskite-based ferroelectrics is attributed to ferroelectrostriction, which is driven by large ferroelectric displacements resulting from the strong covalent nature of the A/B-O bonds [19, 280, 285, 299, 311, 312]. Ferroelectrostriction in perovskite-based relaxor ferroelectrics arises from the enhanced correlations among intra/inter-polar clusters (PNRs) exhibiting ferroelectric (or polar) distortions [142, 313]. The ferroelectric (or polar) distortions responsible for ferroelectrostriction are associated with the freezing of a soft phonon mode corresponding to the zone center of the cubic Brillouin zone ($q = 0,0,0$) [55, 227, 253]. Among various phonon modes corresponding to the Γ-point of the cubic Brillouin zone, a triply degenerate Γ_4^- phonon mode (often known as ferroelectric mode) is responsible for ferroelectric (or polar) ordering. The freezing of Γ_4^- phonon mode along various dimensions leads to various low symmetry phases of $BaTiO_3$ *viz.*, *P*4*mm*, *Amm*2, and *R*3*m* with (a,0,0), (a,a,0), and (a,a,a) order parameter direction (OPD) respectively. Hence, the frozen phonon mode approach (or symmetry mode analysis) can be used to quantify the ferroelectric (or polar) distortions [55, 227, 253]. Most of the prominent relaxor ferroelectrics are Pb-based *viz.*, PZN [281], PMN [284] etc. Due to the harmful effects of Pb on the environment and humans, various alternatives *viz.*, $Ba(Zr,Ti)O_3$ [206], $Ba(Sn,Ti)O_3$[314], $(K,Na)NbO_3$[56], $(K,Na,Ba,Sr)(Nb,Ti)O_3$[15, 22, 62] and other related materials are widely studied.

The alkali niobate-based system *viz.*, $K_{0.5}Na_{0.5}NbO_3$ (KNN50) is widely studied for its enhanced physical responses which is due to the presence of morphotropic phase boundary (MPB) [8, 51, 53, 54, 55, 56]. Orayech *et al.* reported a series of structural phase transitions *viz.*, $R3c \xrightarrow{\approx 135K} Amm2 \xrightarrow{\approx 465K} P4mm \xrightarrow{\approx 700K} Pm\bar{3}m$ as a function of temperature using

X-ray and neutron diffraction data [55]. Moreover, later Kong *et al.* reported another series of phase transitions *viz.*, $Pm \xrightarrow{\approx 471K} P4mm \xrightarrow{\approx 674K} Pm\bar{3}m$, where a monoclinic phase is found to be stable down to the lowest studied temperature [56]. Further, Gupta *et al.*, Kong *et al.*, and Tripathi *et al.* confirmed the monoclinic symmetry at short ranges using Pair Distribution Function (PDF) data [56, 171, 212].

Moreover, the alkaline earth metal-based perovskite *viz.*, $BaTiO_3$ and its solid solutions are also widely studied as a potential alternative to Pb-based materials. The doping of elements like Strontium at the A-site induces disorder/relaxor behavior in the material. Among, various compositions of Sr-doped $BaTiO_3$ *viz.*, $Ba_{(1\text{-}x)}Sr_xTiO_3$, the maximum dielectric response at ambient conditions is observed for x = 0.10 (BST10). BST10 undergoes similar structural phase transitions to that of $BaTiO_3$ *i.e.*, $R3m \rightarrow Amm2 \rightarrow P4mm \rightarrow Pm\bar{3}m$ but with a shift in T_C ($\approx$ 369 K) to lower temperatures [63, 64, 65, 66, 181]. Among other Pb-free alternatives, KNN50 doped $BaTiO_3$ (KBTx) has been studied for its unique structural properties at short and long ranges, leading to the discovery of morphotropic relaxor boundary (MRB) [15]. Moreover, authors have doped Strontium (Sr) at the A-site of KBTx to enhance the disorder/relaxor property of the ceramics [22, 62].

In the present work, we have chosen Pb-free Sr-doped $BaTiO_3$ *viz.*, $Ba_{0.9}Sr_{0.1}TiO_3$ (BST10) as one of the parents due to its maximum dielectric response [63, 64, 65, 66], and KNN50 as the other parent to form a solid solution *viz.*, (1-x)KNN50-xBST10 (KBSTx). We have analyzed the crystal structures at long/short ranges and associated properties for $0.90 \leq x \leq 1.00$ (BST10 end). The crystal structures at long ranges, along with various electrical properties, have been determined for KBSTx (x = 0.90, 0.95, and 1.00) ceramics using X-ray diffraction, dielectric, and P-E loop data. A relaxor behavior is observed for x = 0.90 (KBST90) in temperature-dependent dielectric data. Moreover, the atomic ordering at various length scales (long/intermediate/short) for KBST90 has been determined using temperature-dependent Synchrotron X-ray diffraction, Raman scattering, and pair distribution function data. The ferroelectric displacements at various length scales have been quantified by calculating the amplitude of structural distortion modes using ISODISTORT. In addition, spontaneous volume ferroelectrostriction (SVFS) was calculated using the Debye-Gr*ü*niesen equation.

6.2 Experimental procedure

The KBSTx (x = 0.90, 0.95, and 1.00) ceramics were prepared using solid-state reaction technique. The precursors *viz.*, K_2CO_3 (Sisco Research Laboratories Pvt. Ltd.) (99%), Na_2CO_3 (HIMIDEA Labs) (99.5%), $BaCO_3$ (HIMIDEA Labs) (99%), $SrCO_3$ (HIMIDEA Labs) (99%), Nb_2O_5 (HIMIDEA Labs) (99.9%), and TiO_2 (HIMIDEA Labs) (99%) were pre-heated in an oven at 393 K. The heated powders were weighed as per stoichiometry and mixed *via* milling for 24 hours. After milling, the powder slurry was dried and calcined at 1173 K - 1223 K for 4 hours. The pellets were formed at 8-10 metric tons pressure and sintered at 1423 K - 1473 K for 3 hours. The room temperature X-ray diffraction data has been collected over the 2θ range of 20° to 120° with a step size of 0.02, from Rigaku Miniflex 600 X-ray diffractometer having Cu-K_α radiation. The sintered pellets were electroded with silver paste on both sides for the dielectric and PE loop measurements. The dielectric measurements were carried out using a Keysight LCR meter with frequency and temperature range of 1 kHz–1 MHz and 100 K $\leq$ T $\leq$ 650 K, respectively. For PE loop measurements at 10 Hz frequency, Radiant Technology's Precision LCII Ferroelectric Tester was used. The temperature-dependent Synchrotron X-ray diffraction measurements were performed at the 28-ID-2 (XPD) beamline, in the National Synchrotron Light Source-II (NSLS-II) at Brookhaven National Laboratory (BNL) with λ = 0.1821 Å for the temperature range of 100 K $\leq T \leq$ 500 K. The intermediate- and short-range crystal structure was analyzed using temperature-dependent Raman scattering and Pair Distribution Function (PDF) data. The temperature-dependent Raman spectra were obtained *via* Horiba LabRAM HR Raman spectrometer with an Olympus BX41 microscope attachment with an excitation wavelength of 514.5 nm from a Lexel Model-95 argon ion laser. The samples were placed in a Linkam THMS600 microscope stage for Raman measurements at varying temperatures. A 50x LWD objective lens (N.A. = 0.50) was used to focus the laser beam onto the samples, and the backscattered light was dispersed using a 600 lines/mm grating onto a liquid nitrogen-cooled CCD detector. Data acquisition was carried out with LabSpec v5 software. The laser power at the sample was approximately 0.4 mW, which was confirmed to ensure there were no local heating effects from the laser. The spectral range for this study was selected to span from 80 to 1900 cm^{-1}.

The PDF data was obtained from the high-energy SXRD data, which was reduced to total scattering structure function S(Q), given as follows [208, 211]:

$$S(Q) = 1 + \frac{[I_{\mathrm{coh}}(Q) - \sum c_{\mathrm{i}}|f_{\mathrm{i}}(Q)|^2]}{|\sum f_{\mathrm{i}}(Q)c_{\mathrm{i}}|^2} \tag{6.1}$$

where Q is defined as Q = $4\pi\sin\theta/\lambda$ and is referred as the wave vector, 2θ is the angle between incident and diffracted beams, I_{coh} corresponds to the coherent part of the diffraction data while c_{i} and $f_{\mathrm{i}}(Q)$ are the atomic concentrations and x-ray structure factor of atomic species of i^{th} type. The S(Q) was then transformed to final Pair Distribution Function G(r) *via* Fourier transformation with Q_{max} = 23.6 Å^{-1} [208, 211]:

$$G(r) = \frac{2}{\pi}\int_{Q_{\mathrm{min}}}^{Q_{\mathrm{max}}} Q[S(Q)-1]sin(Qr)dQ \tag{6.2}$$

where Q_{min} = 0.65 Å^{-1}.

Further, the decomposition of phonon modes has been done using the ISODISTORT tool available online [258, 315].

6.3 Results and discussions

6.3.1 XRD analysis of KBSTx ceramics for $0.90 \leq x \leq 1.00$

The long-range crystal structure of KBSTx (x = 0.90, 0.95, and 1.00) ceramics was determined by analyzing the X-ray diffraction data. Figure 6.1 shows the X-ray diffraction pattern of KBSTx ceramics with the evolution of main perovskite peaks *viz.*, {200}, {220}, and {222}. The XRD patterns confirm the formation of a solid solution with a trace amount of impurity (<1%) of the secondary phase *i.e.*, $Na_{13}Nb_{35}O_{94}$ (Space Group: *Pba*2) [255]. For x = 1.00 (BST10), the splitting of main perovskite peaks suggests tetragonal symmetry similar to $BaTiO_3$ with *P*4*mm* space group, while for x = 0.95 (KBST95) and 0.90 (KBST90), the peaks do not split, suggesting cubic symmetry with $Pm\bar{3}m$ space group. Further, the Rietveld refinements of KBSTx ceramics were carried out using the FULLPROF package [239]. The initial parameters for refinements were taken from $BaTiO_3$ crystal structure [181]. The asymmetric unit of BST10 (Space Group: *P*4*mm*) consists of four atoms *viz.*, Ba/Sr, Ti, O1, and O2 associated with 1a ($0,0,0\pm\delta z$), 1b ($0.5,0.5,0.5\pm\delta z$), 1b ($0.5,0.5,0\pm\delta z$), and 2c ($0.5,0,0.5\pm\delta z$) Wyckoff sites respectively. Moreover, the asymmetric unit of KBST95 and KBST90 ceramics (Space Group: $Pm\bar{3}m$) consists of three atoms *viz.*, Ba/Sr/K/Na, Ti/Nb, and O are associated with 1a (0,0,0), 1b (0.5,0.5,0.5), and 3c (0.5,0,0) Wyckoff sites, respectively. The Rietveld patterns for x = 0.90, 0.95, and 1.00 are shown in Fig. 6.2, with insets showing a zoomed-up view of the fitted profiles of the main perovskite peaks. The agreement factors *viz.*, R_{wp}, R_{exp}, and χ^2 obtained after refinement are within the acceptable range, indicating a good fit and thereby suggesting that the obtained structural parameters are reliable. Structural parameters and agreement factors obtained after refinements are mentioned in the tables below (see Tables 6.1, 6.2, and 6.3).

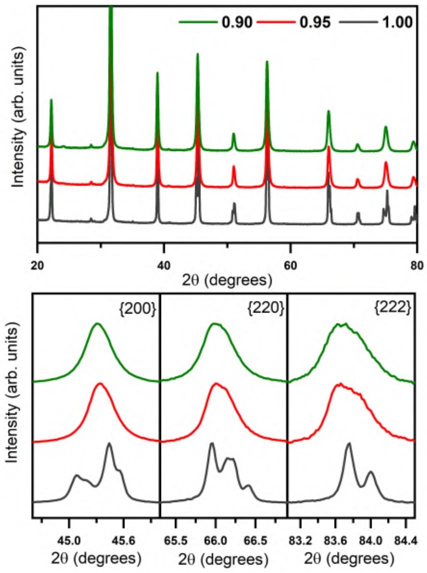

Fig. 6.1 The X-ray diffraction plot of KBSTx (x = 0.90, 0.95, and 1.00) ceramics with the evolution of main perovskite peaks *viz.*, {200}, {220}, and {222}.

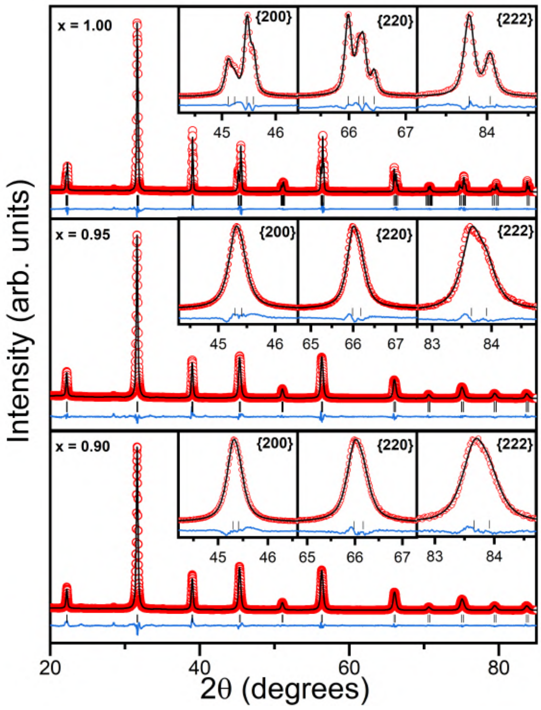

Fig. 6.2 Rietveld fits of KBSTx (x = 0.90, 0.95, and 1.00) ceramics with insets showing the fits of {200}, {220}, and {222} peaks. The simulated patterns are depicted by the continuous black line, while the observed patterns are shown by the open red circles. The Bragg reflections are indicated by vertical black bars, and the difference between the observed and simulated patterns is represented by the continuous blue line at the bottom.

Table 6.1 Various structural parameters and agreement factors obtained from the Rietveld refinements of the X-ray diffraction patterns (at ambient conditions) for x = 1.00 *via* tetragonal (*P*4*mm*) model.

Rietveld Refinement				
Space group: *P*4*mm*				
Atoms	x	y	z	B_{iso}(Å^2)
Ba/Sr	0.0000	0.0000	0.0000	0.0340(100)
Ti	0.5000	0.5000	0.4853(13)	0.1310(220)
O1	0.5000	0.5000	0.0109(80)	0.0440(143)
O2	0.5000	0.0000	0.5144(41)	0.2520(84)
a=3.98658(2)Å, c=4.01580(3)Å				
V=63.822(1)Å^3				
Agreement factors: R_{wp}=6.81, R_{exp}=2.24, χ^2=6.79				

Table 6.2 Various structural parameters and agreement factors obtained from the Rietveld refinements of the X-ray diffraction patterns (at ambient conditions) for x = 0.95 *via* cubic ($Pm\bar{3}m$) model.

Rietveld Refinement				
Space group: $Pm\bar{3}m$				
Atoms	x	y	z	B_{iso}(Å^2)
K/Na/Ba/Sr	0.0000	0.0000	0.0000	0.1070(50)
Nb/Ti	0.5000	0.5000	0.5000	0.6860(130)
O	0.5000	0.0000	0.5000	0.2010(230)
a=4.00088(1)Å				
V=64.042(1)Å^3				
Agreement factors: R_{wp}=4.16, R_{exp}=2.28, χ^2=3.33				

6.3.2 Microstructure analysis of KBST90 ceramics

We have obtained the Scanning Electron Microscope (SEM) data from JCM-6000 Plus BenchTop SEM Neoscope. The grain size and porosity of KBST90 ceramics were calculated using the microscopic image shown below (see Fig. 6.3). The average grain size is 1.79 μm, and the porosity is 2.88 %, suggesting high density of the ceramics. The SEM picture of KBST90 depicts the homogeneous formation of ceramic with high density.

Table 6.3 Various structural parameters and agreement factors obtained from the Rietveld refinements of the X-ray diffraction patterns (at ambient conditions) for x = 0.90 *via* cubic ($Pm\bar{3}m$) model.

Rietveld Refinement				
Space group: $Pm\bar{3}m$				
Atoms	x	y	z	B_{iso}(Å^2)
K/Na/Ba/Sr	0.0000	0.0000	0.0000	0.1140(60)
Nb/Ti	0.5000	0.5000	0.5000	0.7730(130)
O	0.5000	0.0000	0.5000	0.1930(240)
a=4.00137(2)Å				
V=64.066(1)Å^3				
Agreement factors: R_{wp}=4.30, R_{exp}=2.25, χ^2=3.67				

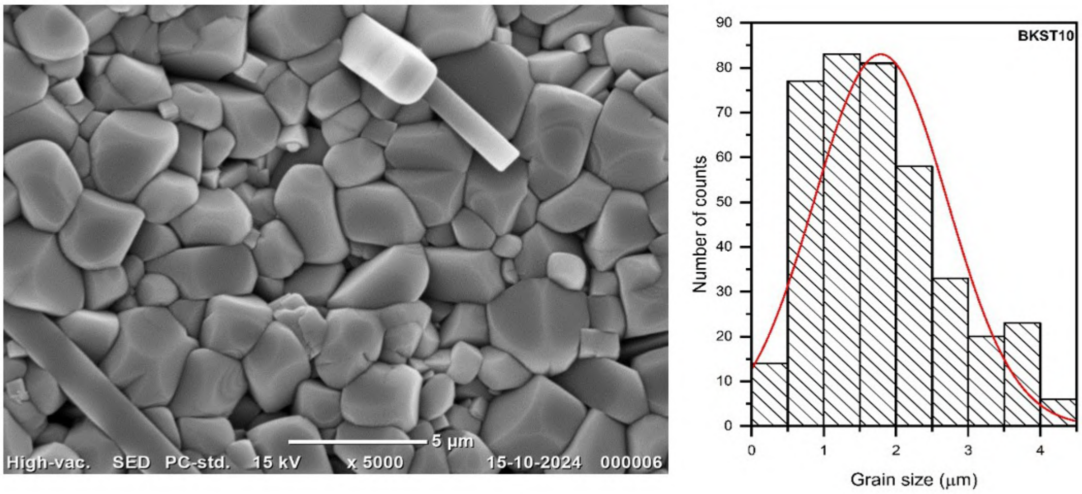

Fig. 6.3 SEM picture of KBST90 ceramics along with histogram depicting the grain size distribution in KBST90 ceramics.

6.3.3 Dielectric and PE loops of KBSTx ceramics for 0.90 $\leq x \leq$ 1.00

The temperature-dependent dielectric measurements for all the compositions have been carried out for a wide temperature range (100 K $\leq T \leq$ 650 K). Figures 6.4(a)-(c) show the temperature-dependent dielectric behavior (real (ε') and imaginary (ε'') part) for x = 1.00 (BST10), 0.95 (KBST95), and 0.90 (KBST90) ceramics at 100 kHz. For BST10, three dielectric peaks have been observed, which are attributed to the three phase transitions *viz.*, $Pm\bar{3}m \xrightarrow{\approx 382K} P4mm \xrightarrow{\approx 274K} Amm2 \xrightarrow{\approx 192K} R3m$ similar to those of $BaTiO_3$ with

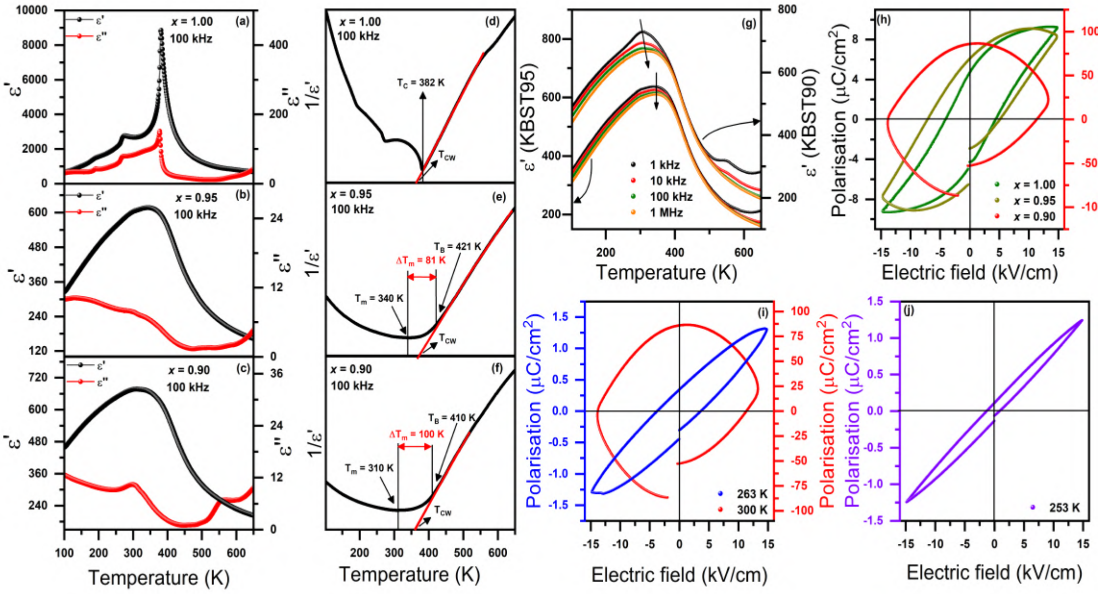

Fig. 6.4 Electrical properties of KBST*x* ceramics including (a)-(c) The temperature-dependent real (ε') and imaginary (ε'') part of KBST*x* ceramics, (d)-(f) the plot between the inverse of the real part of dielectric constant and temperature *i.e.*, $1/\varepsilon'$ vs. T for x = 1.00, 0.95, and 0.90 ceramics at 100 kHz, (g) the frequency-dependent plot between real part of dielectric constant (ε') with temperature for x = 0.95 and 0.90, (h) P-E loops for KBST*x* ceramics, and (i)-(j) temperature-dependent P-E loops for KBST90 ceramics at 253 K, 263 K, and 300 K.

a decrease in T_C [172, 316]. A single broad and diffuse dielectric peak is observed with increasing KNN50 content *i.e.*, for KBST95 and KBST90 ceramics, suggesting the presence of a diffuse phase transition. Additionally, T_m shifts towards room temperature with increasing KNN50 content (see Figs. 6.4(d)-(f)). The normal ferroelectrics follow Curie-Weiss law above Curie temperature while the dielectric behavior of disordered ferroelectrics (exhibiting diffused dielectric peak) deviates away from Curie-Weiss law below a certain temperature referred to as Burns temperature (T_B) [5, 22, 257]. The nucleation and growth of polar nano regions (PNRs) begins below the Burns temperature [5, 117, 142]. The diffuseness of the dielectric peak can be analyzed/quantified by calculating the deviation from Curie-Weiss law (ΔT_m), which is given as [22, 256]:

$$\Delta T_{\mathrm{m}} = T_{\mathrm{B}} - T_{\mathrm{m}} \tag{6.3}$$

where T_B denotes Burns temperature, and T_m is the temperature corresponding to the dielectric maximum. Figures 6.4(d)-(f) represent the plot between the inverse of the real part of dielectric permittivity and temperature ($1/\varepsilon'$ vs. T) and depict the diffuseness (ΔT_m) of the dielectric peaks with increasing KNN50 content. For BST10, the dielectric behavior follows the Curie-Wiess law. On the other hand, for KBST95, ΔT_m = 81 K while for KBST90, ΔT_m = 100 K, which implies an increase in the diffuseness of the dielectric peak and hence the disorder in the system with increasing KNN50 content [22], which is further supplemented by PE loops.

Figure 6.4(h) represents the PE loops of KBST*x* ceramics. For BST10, the loop dictates ferroelectric behavior similar to $BaTiO_3$ [317], while the shape of the loop changes with increasing KNN50 content. Ferroelectric (FE) loops for KBST95 and KBST90 ceramics depict increasing disorder in the system, finally demonstrating a linear lossy dielectric behavior for KBST90 ceramics [290]. Hence, the maximum disorder is observed for KBST90 ceramics, which is further analyzed for its relaxor behavior. Figure 6.4(g) depicts the frequency-dependent behavior of the real part of the dielectric constant as a function of temperature. A frequency dispersion of $\Delta T \approx 6$ K has been observed in KBST90 ceramics, while KBST95 ceramics do not exhibit any frequency dispersion (see Fig. 6.4(g)). This suggests that KBST90 is a potential relaxor, while KBST95 exhibits only a diffuse phase transition. Moreover, Figs. 6.4(i)-(j) depicts the temperature-dependent P-E loops for KBST90. It is clearly evident from the Figs. 6.4(i)-(j) that the shape of the loop changes on lowering temperatures dictating the transformation of linear lossy dielectric to a relaxor like behavior suggesting enhancement in cationic ordering [290, 313].

6.3.4 SXRD analysis and zero thermal expansion in KBST90 ceramics

Owing to the relaxor behavior observed for KBST90 ceramics, the temperature-dependent evolution of the long-range crystal structure of KBST90 has been analyzed. Figure 6.5(a)-(c) depicts the evolution of the main perovskite peaks *viz.*, {200}, {220}, and {222} observed in the SXRD pattern of KBST90 ceramic for a wide temperature range (100 K $\leq T \leq$ 500 K). The peaks do not split and exhibit a singlet nature throughout the temperature range, which suggests the presence of cubic symmetry down to the lowest studied temperature. The cubic symmetry (Space Group: $Pm\bar{3}m$) is confirmed by analyzing the SXRD data using the Rietveld refinement program available at FULLPROF suite [239]. Moreover, Fig. 6.5(d) depicts the volume as a function of temperature for KBST90 ceramics. The volume deviates from the linear behavior below the Burns temperature ($T_B \approx 410$ K), which is determined using the inverse of temperature-dependent dielectric data (see Fig. 6.4(f)). The volume begins to saturate at low temperatures, indicating zero thermal expansion in the material.

The nearly temperature-independent volume observed at low temperatures for KBST90 ceramics suggests zero thermal expansion (ZTE) in the material (see Fig. 6.5(d)). The ZTE is quantified using the volumetric coefficient of thermal expansion (α_V), which is defined as follows [19]:

$$\alpha_{\mathrm{V}} = \frac{1}{V}\frac{\partial V}{\partial T} \tag{6.4}$$

where V corresponds to volume at temperature T [17, 19]. For cubic systems, the volumetric thermal expansion coefficient (α_{V}) is three times the linear thermal expansion coefficient (α_l), *i.e.*, $\alpha_V = 3\alpha_l$ [19]. For KBST90 ceramics, the calculated linear thermal expansion coefficient (α_l) ranges between $0.623 - 10.109 \times 10^{-6}$ K^{-1} (100 K-500 K), which suggests the ZTE behavior in KBST90 ceramic [313].

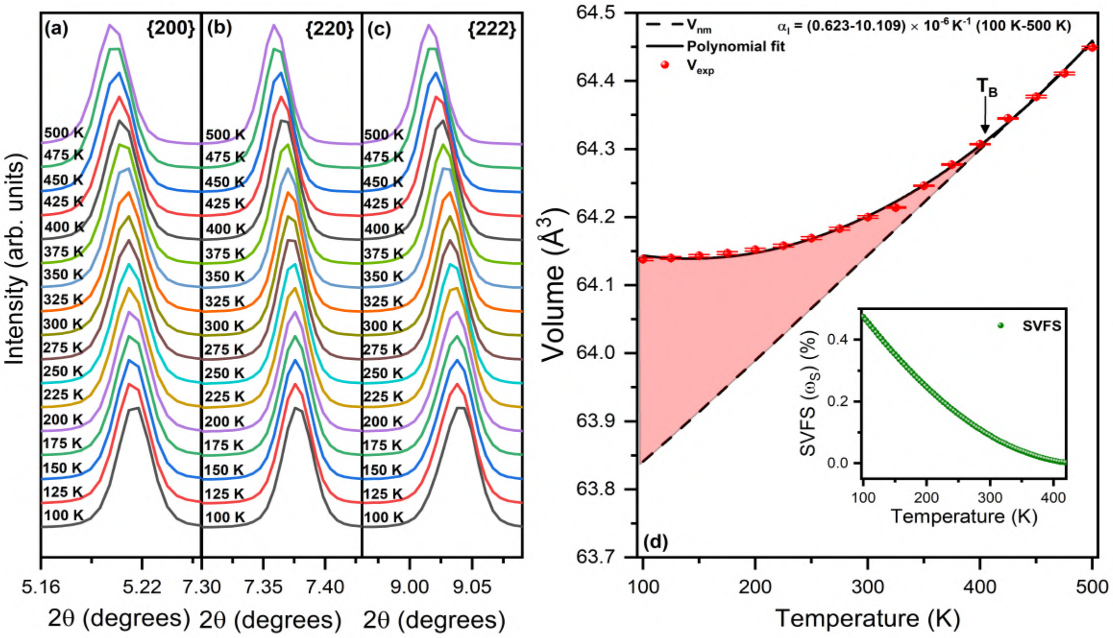

Fig. 6.5 (a)-(c) Temperature-dependent evolution of main perovskite peaks *viz.*, {200}, {220}, and {222} of KBST90 ceramics for 100 K $\leq T \leq$ 500 K, (d) Temperature-dependent evolution of volume for KBST90 ceramics. The symbols represent the experimental volume, whereas solid and dashed lines represent the polynomial fit of experimental volume and nominal volume (V_{nm}), respectively. The inset shows the temperature-dependent evolution of Spontaneous Volume Ferroelectrostriction (SVFS) calculated using interpolated volume data.

As discussed earlier, the NTE/ZTE in perovskite based materials results due to ferroelectrostriction. The ferreoelctrostriction causes volume gain (or Ferroelectrovolume Effect) [284] in the material, which can be quantified using spontaneous volume ferroelectrostriction (SVFS), which is defined as follows [19, 280, 299]:

$$\omega_S = \frac{V_{\mathrm{exp}} - V_{\mathrm{nm}}}{V_{\mathrm{nm}}} \times 100\% \tag{6.5}$$

where ω_S represents SVFS, V_{exp}, and V_{nm} correspond to experimental and nominal volume, respectively. V_{exp} is obtained from the lattice parameter after refinement, while V_{nm} is obtained after fitting the experimental volume using the Debye-Gr*ü*niesen equation in the temperature range of 400 K $\leq T \leq$ 500 K as the deviations begin near the Burns temperature ($T_B \approx 410$ K) [17, 19, 318]. Here, the Debye-Gr*ü*niesen equation is given as follows:

$$V(T) \cong V_0 + 9K\gamma k_B NT \frac{T^3}{\theta_D^3} \int_0^{\theta_D/T} \frac{x^3}{e^x - 1} dx \qquad (6.6)$$

In this equation, $V(T)$ represents the unit cell volume at temperature T, V_0 represents the unit cell volume at 0 K, γ stands for the Gr*ü*neisen parameter, K denotes the isothermal compressibility, k_B represents the Boltzmann constant, N indicates the number of atoms in the primitive unit cell, and θ_D signifies the Debye temperature. The Debye temperature (θ_D) and the volume at 0 K (V_0) are determined to be 150 K and 63.841 $\mathring{A}^3$, respectively. The experimental volume shows a deviation from the nominal volume obtained from fitting, indicating a volume gain for KBST90.

Figure 6.5(d) depicts the ZTE behavior of KBST90 ceramics. The volume gain arising from the ferroelectrostriction can be clearly observed. The inset of the figure depicts the evolution of SVFS (ω_S) with temperature. The SVFS (or ferroelectrostriction) increases with decreasing temperatures. The increase in SVFS suggests an increase in ferroelectrostriction, consequently resulting in ZTE in the material. Furthermore, the presence of ZTE in KBST90 ceramics is attributed to the relaxor behavior of the material having distinct atomic ordering at various length scales, which will be discussed in the following sections.

6.3.5 Raman analysis of KBST90 ceramics

Owing to the relaxor behavior of KBST90 ceramics, the presence of PNRs is obvious. SXRD, Raman scattering, and Pair distribution function are the unique techniques used to analyze the symmetry of the materials at different length scales [244]. Temperature-dependent Raman spectra have been obtained to analyze the symmetry of KBST90 ceramics at intermediate ranges. Figure 6.6 depicts the evolution of Raman spectra at 77 K, 300

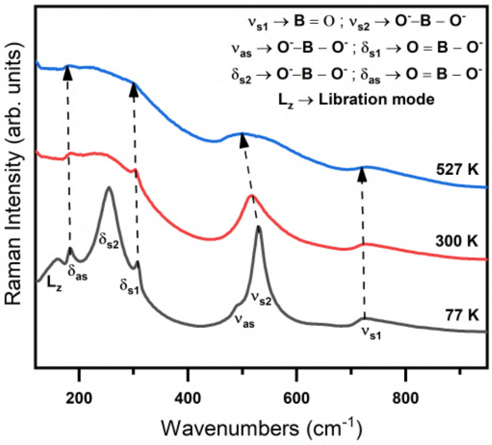

Fig. 6.6 The Raman spectra of KBST90 ceramics at 77 K, 300 K, and 527 K. Description of various modes has been mentioned on the top right of the figure [20, 21] also in Table 6.4.

K, and 527 K. The long-range structure of KBST90 ceramics is cubic (Space Group: $Pm\bar{3}m$) with five triply degenerate phonon modes [262]. Among these, there is one triply degenerate acoustic phonon mode (T_{1u}), and the remaining four are optical phonon modes, which comprise three polar T_{1u} mode and one nonpolar T_{2u} mode *i.e.*, $T_{2u} + 3T_{1u}$ [262]. All these phonon modes are Raman inactive, yet we observe Raman peaks in the spectra, which suggests the presence of local distortions (or PNRs) [262]. The observed Raman spectra of KBST90 ceramics feature seven bands (see Table 6.4) similar to the rhombohedral phase of $BaTiO_3$ [20, 21]. Among these seven bands, six correspond to the internal vibrations of BO_3^{2-} anion, while the seventh band (or lowest frequency band) corresponds to libration mode of BO_6 octahedra [20, 319].

The presence of all these bands in the Raman spectra of KBST90 confirms the rhombohedral symmetry. The six modes corresponding to internal vibrations of BO_3^{2-} are divided into two categories *viz.*, stretching modes or high-frequency modes (denoted by ν) and bending modes or low-frequency modes (denoted by δ). Both of the modes could be symmetric or asymmetric, represented by "s" or "as" respectively in the subscript [20, 21]. The presence of B=O stretching vibrations (ν_{s1} peak) around 727 cm^{-1} is clear evidence of

Table 6.4 Description of various Raman modes observed in temperature-dependent Raman spectra of KBST90 ceramics, where "s" and "as" in the subscript represent symmetric and asymmetric nature of modes, respectively.

Symmetry	
Rhombohedral	
Peak Position (cm^{-1})	Assignment
727	ν_s (B=O)
529	ν_s (O^--B-O^-)
491	ν_{as} (O^--B-O^-)
306	δ_s (O=B-O^-)
254	δ_s (O^--B-O^-)
183	δ_{as} (O=B-O^-)
160	L_Z

the polar distortions in BO_6 octahedra [20]. This peak remains present in all three studied temperatures, confirming the existence of polar distortions up to the highest temperature [20, 306, 307]. Further, the symmetry of KBST90 ceramics at different length scales has been analyzed/confirmed using temperature-dependent PDF data, which will be discussed in the next section.

6.3.6 PDF analysis of KBST90 ceramics

The symmetry of KBST90 ceramics at various length scales *viz.*, short and intermediate ranges can be confirmed using PDF analysis/refinements. We have determined the symmetry of KBST90 ceramics at various length scales and three different temperatures *viz.*, 100 K, 300 K, and 500 K. Figure 6.7 depicts the PDF fits of KBST90 ceramics at 100 K at different length scales for rhombohedral (orange line) and monoclinic (green line) symmetry. Owing to the rhombohedral symmetry concluded from Raman spectra, $R3m$ $[a^0_+a^0_+a^0_+]$ space group was used to refine the PDF data for the range $1.7\ \text{Å} \leq r \leq 10\ \text{Å}$. Various misfits were observed at different bond lengths, as indicated by the black arrow in Fig. 6.7(a). Thereafter, PDF data was fitted using monoclinic symmetry (Space Group: Pm $[a^0_+b^0_+c^0_0]$) at short ranges ($1.7\ \text{Å} \leq r \leq 10\ \text{Å}$). Here, it is important to note that this

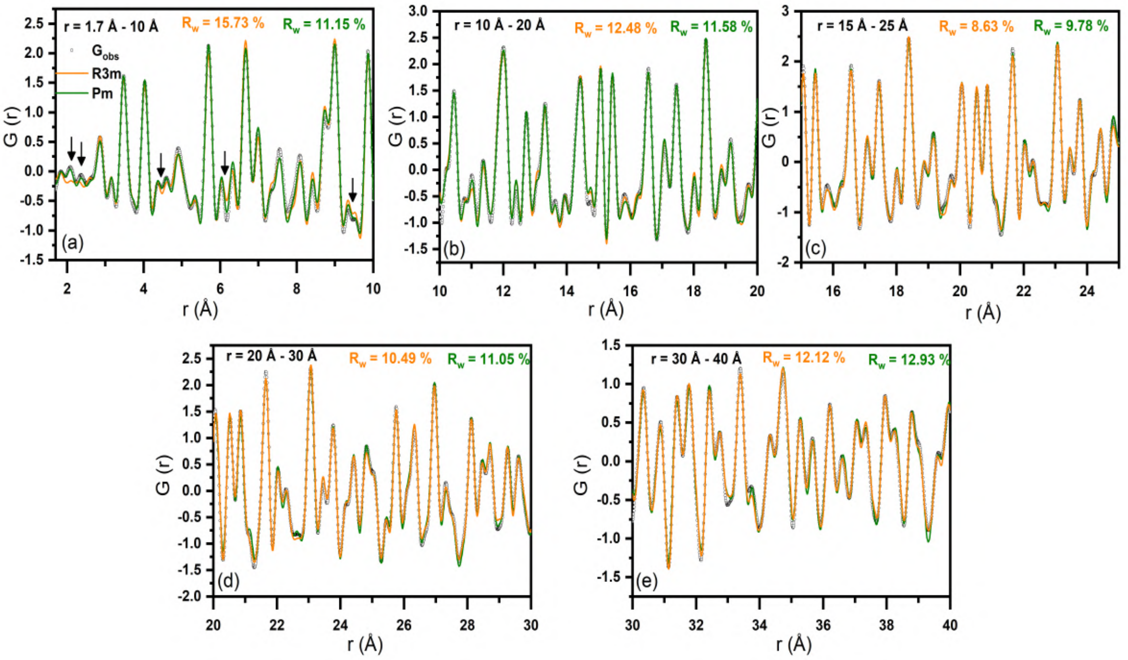

Fig. 6.7 The fitting of PDF profiles at various length scales *viz*., (a) 1.7 Å- 10 Å, (b) 10 Å- 20 Å, (c) 15 Å- 25 Å, (d) 20 Å- 30 Å and, (e) 30 Å- 40 Å using *Pm* and *R*3*m* space groups for KBST90 ceramics. The black open circles denote observed PDF data, while orange and green lines correspond to *R*3*m* and *Pm* fit, respectively. The arrow represents the misfit observed by the *R*3*m* space group at $r \leq 10$ Å.

monoclinic phase is reported for KNN50 both at long and short ranges stable for wide temperature ranges (100 K $\leq T \leq$ 471 K) [56, 171]. This is reminiscent of an earlier report on $NaNbO_3$ published in Physical Review B [27]. The PDF fit significantly improves with the *Pm* space group and gives a lower R_w value for 1.7 Å $\leq r \leq$ 10 Å in comparison to the *R*3*m* space group (see Fig. 6.7(a)), confirming a monoclinic (*Pm*) symmetry at short ranges ($r \leq$ 10 Å).

Moreover, at higher interatomic distances *i.e*., for $r >$ 10 Å (intermediate ranges), the PDF data has been fitted using the *Pm* and *R*3*m* space groups. It is clearly observed that at intermediate ranges ($r >$ 10 Å), the *R*3*m* phase fits the PDF data better than the *Pm* phase, with lower R_w values obtained for the *R*3*m* phase at different length scales *viz*., 15 Å $\leq r \leq$ 25 Å, 20 Å $\leq r \leq$ 30 Å, and 30 Å $\leq r \leq$ 40 Å (see Figs. 6.7(c)-(e)). This analysis of PDF fits across various length scales at intermediate ranges confirms the gradual transformation from *Pm* to *R*3*m* phase at higher length scales *i.e.*, intermediate ranges. Now, as discussed in the previous section, a rhombohedral symmetry has been confirmed at intermediate ranges at all temperatures (77 K, 300 K, and 527 K) by Raman scattering. This is further validated *via* PDF refinements at intermediate ranges, where a rhombohedral phase (*R*3*m*) gives a better fit relative to the *Pm* phase observed at short ranges ($r \leq 10$ Å). Hence, PDF analysis at a higher length scale (intermediate ranges) conforms well with the observed Raman spectra.

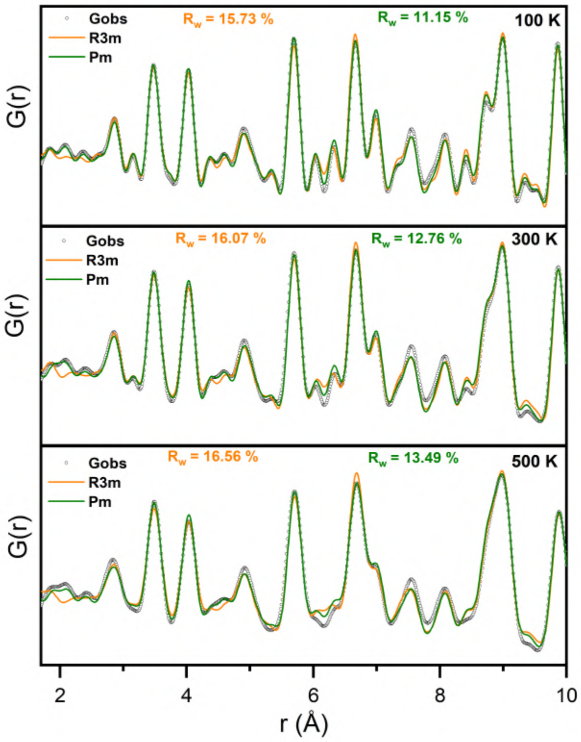

Fig. 6.8 Fitting of the temperature-dependent PDF profiles of KBST90 ceramics using monoclinic (*Pm*) and rhombohedral (*R*3*m*) space groups for 1.7 Å $\leq r \leq$ 10 Å at 100 K, 300 K, and 500 K. The open circles represent observed PDF data, while orange and green lines represent PDF fits for rhombohedral (*R*3*m*) and monoclinic (*Pm*) space groups.

Furthermore, the PDF refinements have also been done for 300K and 500K at short and intermediate ranges using monoclinic and rhombohedral phases, respectively. The refinements at short ranges (1.7 Å $\leq r \leq$ 10 Å) with monoclinic (*Pm*) and rhombohedral

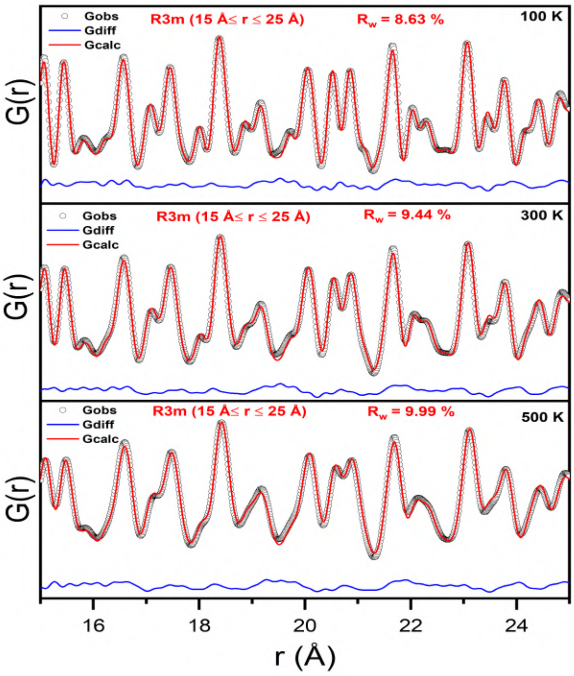

Fig. 6.9 Fitting of the temperature-dependent PDF profiles of KBST90 ceramics using rhombohedral ($R3m$) space groups for 15 Å $\leq r \leq$ 25 Å at 100 K, 300 K, and 500 K. The open circle represents the observed PDF data, while the red line represents the calculated PDF data, and the blue line represents the difference between observed and calculated data.

($R3m$) space groups at 100 K, 300 K, and 500 K are shown in Fig. 6.8. The monoclinic symmetry provides better fits (with lower R_w values) for $r \leq 10$ at all the temperatures (see Fig. 6.8), confirming monoclinic phase (Pm) at short ranges for a wide temperature range. Moreover, the rhombohedral phase was confirmed at intermediate ranges using Raman scattering (see Fig. 6.6) and PDF data (see Fig. 6.9) for a wide temperature range (100 K $\leq T \leq$ 500 K). Further, the structural parameters obtained after PDF refinements at short and intermediate ranges (see Tables 6.5, 6.6, and 6.7) were used for symmetry mode analysis in the next section.

6.3.7 Frozen phonon mode approach

The static atomic displacements are held responsible for distortions within the unit cell [227, 252]. In order to quantify these distortions, the frozen phonon mode approach has

Table 6.5 Various structural parameters obtained for KBST90 ceramics from the PDF refinements at 100 K for different length scales.

PDF Refinement								
	Space group: *Pm* (1.7 Å$\leq r \leq$ 10 Å)				Space group: *R*3*m* (15 Å$\leq r \leq$ 25 Å)			
Atoms	x	y	z	U_{equiv}(Å^2)	x	y	z	U_{equiv}(Å^2)
K/Na/Ba/Sr	0.9854(71)	0.0000	0.0245(50)	0.0021(8)	-0.0099(14)	-0.0099(14)	-0.0099(14)	0.0026(3)
Nb/Ti	0.4980(44)	0.5000	0.5403(2)	0.0024(16)	0.4795(16)	0.4795(16)	0.4795(16)	0.0024(26)
O1	0.4810(57)	0.5000	0.0045(2)	0.0104(46)	0.5198(71)	0.5198(71)	0.0202(100)	0.0138(19)
O2	0.9777(26)	0.5000	0.5035(63)	0.0127(21)				
O3	0.6213(78)	0.0000	0.4855(61)	0.0146(75)				
	a=4.028(1)Å, b=4.019(7)Å, c=4.024(1)Å,				a=4.024(1)Å			
	β=90.295(1)				α=89.934(58)			
	Agreement factor R_w = 11.15 %				Agreement factor R_w = 8.63 %			

Table 6.6 Various structural parameters obtained for KBST90 ceramics from the PDF refinements at 300 K for different length scales.

PDF Refinement								
	Space group: *Pm* (1.7 Å$\leq r \leq$ 10 Å)				Space group: *R*3*m* (15 Å$\leq r \leq$ 25 Å)			
Atoms	x	y	z	U_{equiv}(Å^2)	x	y	z	U_{equiv}(Å^2)
K/Na/Ba/Sr	0.9842(85)	0.0000	0.0219(63)	0.0045(15)	-0.0085(22)	-0.0085(22)	-0.0085(22)	0.0056(1)
Nb/Ti	0.4979(6)	0.5000	0.5395(51)	0.0027(15)	0.4791(24)	0.4791(24)	0.4791(24)	0.0033(1)
O1	0.4748(35)	0.5000	0.0052(31)	0.0126(17)	0.5185(77)	0.5185(77)	0.0194(120)	0.0179(27)
O2	0.9732(6)	0.5000	0.5040(75)	0.0135(64)				
O3	0.6187(74)	0.0000	0.4816(59)	0.0151(82)				
	a=4.026(3)Å, b=4.024(10)Å, c=4.033(3)Å,				a=4.028(1)Å			
	β=90.452(41)				α=89.981(110)			
	Agreement factor R_w = 12.76 %				Agreement factor R_w = 9.44 %			

Table 6.7 Various structural parameters obtained for KBST90 ceramics from the PDF refinements at 500 K for different length scales.

PDF Refinement								
	Space group: *Pm* (1.7 Å$\leq r \leq$ 10 Å)				Space group: *R*3*m* (15 Å$\leq r \leq$ 25 Å)			
Atoms	x	y	z	U_{equiv}(Å^2)	x	y	z	U_{equiv}(Å^2)
K/Na/Ba/Sr	0.9859(20)	0.0000	0.0149(84)	0.0071(25)	-0.0082(35)	-0.0082(35)	-0.0082(35)	0.0084(1)
Nb/Ti	0.4949(18)	0.5000	0.5354(71)	0.0044(27)	0.4782(38)	0.4782(38)	0.4782(38)	0.0053(15)
O1	0.4811(75)	0.5000	0.0008(130)	0.0262(30)	0.5152(84)	0.5152(84)	0.0207(19)	0.0273(54)
O2	0.9865(120)	0.5000	0.4978(51)	0.0139(26)				
O3	0.6145(87)	0.0000	0.4841(51)	0.0230(126)				
	a=4.026(3)Å, b=4.043(17)Å, c=4.032(3)Å,				a=4.033(1)Å			
	β=90.467(45)				α=89.999(200)			
	Agreement factor R_w = 13.49 %				Agreement factor R_w = 9.99 %			

been considered. The freezing of phonon mode(s) associated with the cubic Brillouin zone along certain dimensions with equal/unequal magnitudes leads to the stabilization of a low symmetry phase. The phonon mode responsible for symmetry breaking is referred to as primary, while other phonon mode(s) are referred to as secondary [227, 232, 252]. A cubic phase ($Pm\bar{3}m$ space group) with lattice parameter a = 4.00934 Å while A-site, B- site, and

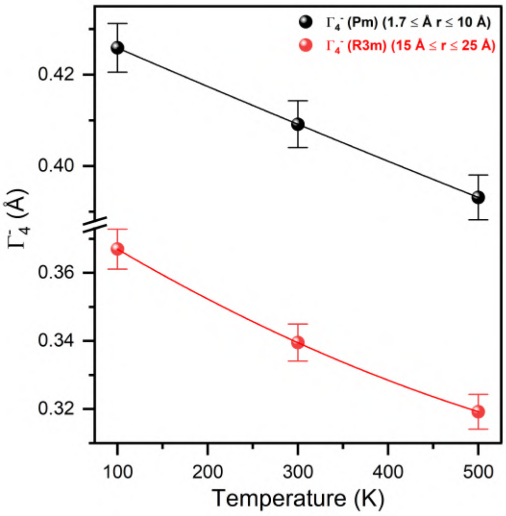

Fig. 6.10 Temperature-dependent evolution of the amplitude of the ferroelectric phonon mode (Γ_4^-) for *Pm* (1.7 Å $\leq r \leq$ 10 Å), and *R*3*m* (15 Å $\leq r \leq$ 25 Å) space group.

Oxygen atoms are fixed at 1b (0.5,0.5,0.5), 1a (0,0,0), and 3d (0.5,0,0) Wyckoff positions respectively is used as the high symmetry phase. The high symmetry phase is related to the low symmetry phase *via* a group-subgroup relation given as follows [232, 236, 253]:

$$r(\mu,i) = r_0(\mu,i) + u(\mu,i) \tag{6.7}$$

where r(μ, i) corresponds to the position of μ (= 1, 2, 3, 4,....) atom of low symmetry space group, $r_0(\mu$, i) corresponds to atomic positions of high symmetry and u(μ, i) are the static displacements associated to low symmetry phase. Now, in order to quantify the ferroelectric distortions present in the structure at short and intermediate ranges, the amplitude of symmetry adapted distortions were calculated using ISODISTORT [258, 315]. As discussed earlier, a monoclinic (*Pm*) and rhombohedral (*R*3*m*) phase is observed for short and intermediate ranges, respectively. The monoclinic and rhombohedral phase results from the freezing of the triply degenerate ferroelectric phonon mode (Γ_4^-) having Order Parameter Direction (OPD) (a,0,b) and (a,a,a), respectively.

Figure 6.10 depicts the variation of the amplitude of ferroelectric phonon mode (Γ_4^-) as a function of temperature for a short (1.7 Å $\leq r \leq$ 10 Å) and intermediate range (15 Å $\leq r$ $\leq$ 25 Å). The amplitude of the ferroelectric (FE) phonon mode quantifies the ferroelectric distortions present in PNRs. Moreover, the amplitude of FE phonon mode increases on lowering temperatures (see Fig. 6.10). This increase in the amplitude of the FE phonon mode can be linked with an increase in the ferroelectric polarization of PNRs. Therefore, enhanced ferroelectric polarization (amplitude of Γ_4^-) at low temperatures can be attributed to thermally induced ferroelectrostriction (volume gain), which can be considered as the origin of zero thermal expansion in the material.

6.4 Conclusion

In conclusion, distinct atomic ordering (non-polar/polar) has been observed at various length scales in a ferroelectric relaxor *viz.*, $0.10(K_{0.5}Na_{0.5}NbO_3)$-$0.90(Ba_{0.9}Sr_{0.1}TiO_3)$ (KBST90), determined and quantified by analyzing temperature-dependent real (PDF) and reciprocal space (SXRD) data in conjunction with symmetry mode analysis. Successive ferroelectric phases *viz.*, monoclinic (*Pm*) and rhombohedral (*R*3*m*) have been identified at short- and intermediate ranges *via* integrated analysis of temperature-dependent Raman scattering and PDF data. On the contrary, a centrosymmetric non-polar cubic phase ($Pm\bar{3}m$) has been confirmed at long ranges using temperature-dependent SXRD. The ferroelectric (or polar) distortions observed at short and intermediate ranges have been quantified in terms of the amplitude of ferroelectric phonon mode Γ_4^-. The amplitude of Γ_4^- phonon mode increases with the decrease in temperatures, suggesting an increase in ferroelectric polarization on lowering temperatures. This increase in ferroelectric polarization at short/intermediate ranges, along with an increase in intra/inter-polar cluster interactions, has been attributed to the volume gain (ferroelectrostriction) in the material at low temperatures. Thus, ferroelectrostriction results in Zero Thermal Expansion (ZTE) with a linear coefficient of thermal expansion ranging from 0.623 $-$10.109 × 10^{-6} K^{-1} (100 K – 500 K).

In the next chapter, we will explore the atomic ordering and associated physical properties for the intermediate region of KBSTx ceramics ($0.20 \leq x \leq 0.90$).